RSC Advances

PAPER

View Article Online
View Journal | View Issue

Cite this: *RSC Adv.*, 2021, **11**, 13386

Tribocatalytic degradation of dyes by tungsten bronze ferroelectric $Ba_{2.5}Sr_{2.5}Nb_8Ta_2O_{30}$ submicron particles†

Chaozhong Sun,[a] Xiaoying Guo,[a] Changzheng Hu,*[a] Laijun Liu,[a] Liang Fang,[a] Zhenxiang Cheng*[b] and Nengneng Luo[ac]

Received 24th December 2020
Accepted 2nd April 2021

DOI: 10.1039/d0ra10807c

rsc.li/rsc-advances

Searching for a new approach in environmental remediation in terms of dye degradation is important in industrialized society. In this work, ferroelectric $Ba_{2.5}Sr_{2.5}Nb_8Ta_2O_{30}$ (BSNT) submicron powders prepared by the high-temperature solid-phase method are used for dye degradation under magnetic stirring. The dye in solution can be quickly degraded by magnetically stirring BSNT submicron particles in the dark in ambient temperature conditions. More importantly, the degradation efficiency can be greatly improved through simple modification of the stirring materials from glass to polypropylene, with a degradation efficiency of rhodamine B as high as 99% in 1.5 h at a gentle stirring speed of 300 rpm. Control experiments reveal that the degradation of the dye is mainly contributed by the friction between BSNT submicron particles and PTFE stirring rods. It is proposed that the friction between ferroelectric polar BSNT particles and PTFE causes charge transfer and induces a non-zero internal electric field to drive the separation of electron–hole pairs in BSNT particles, resulting in a novel tribocatalytic degradation of the dye, which is proven by the detection of $^{\bullet}OH$ and $^{\bullet}O_2^-$ intermediate products during stirring. This work demonstrates that the friction energy of ferroelectric materials with strong polarization is an alternative approach for highly efficient dye degradation.

1. Introduction

The colorful world created by the application of dyes in the fields of textiles and printing plays an important role in enriching people's material and cultural lives.[1,2] However, a large amount of dye wastewater is generated, which has the characteristics of large volume, complex components, deep chroma, and difficult degradation. Moreover, most dyes are toxic and carcinogenic, seriously polluting the natural environment.[3,4] The effective treatment of dye wastewater has always been a difficulty for industry. In recent years, some advanced oxidation technologies have been developed to degrade dye wastewater. Ferroelectric materials show great potential in this regard.[5,6] For ferroelectric materials at the micron or nanoscale, as the particle size decreases, the specific surface area is significantly increased, which can bring rich surface, interface and catalytic effects.[7] For example, micro- and nanostructured ferroelectric materials are used to absorb solar energy, in which electrons and holes are generated and separated to react with water under light irradiation to produce strong active substances, such as hydroxyl radicals ($^{\bullet}OH$) and superoxide radicals ($^{\bullet}O_2^-$), causing the dye to decompose.[8] Currently reported ferroelectric photocatalysts such as $Ag_{10}Si_4O_{13}$,[9] $KNbO_3$ (ref. 10) and $BaTiO_3$ (ref. 11) can show excellent dye decomposition performance under sunlight. Similar to the photoelectrochemical effect of photocatalysts, the piezoelectric effect and pyroelectric effect of ferroelectric materials also have the ability to convert vibrational energy and temperature variations into chemical energy. Therefore, mechano-electrochemical and pyro-electrochemical effects have been demonstrated in successful dye decomposition,[12] water splitting[13] and sterilization.[14] In addition to photoelectrochemical, mechano-electrochemical and pyro-electrochemical effects, ferroelectric materials also show great potential for novel mechanically driven tribo-electrochemical effects for water treatment. Recently, Li *et al.*[15] successfully used the ferroelectric material $Ba_{0.75}Sr_{0.25}TiO_3$ nanopowder to collect the triboelectric energy produced by friction to drive the catalytic degradation of dye molecules in dye wastewater. In summary, micro/

[a]*Guangxi Key Laboratory of Optical and Electronic Materials and Devices, Key Laboratory of New Processing Technology for Nonferrous Metals and Materials, Ministry of Education, College of Material Science and Engineering, Guilin University of Technology, Guilin 541004, China. E-mail: huchzh@foxmail.com*

[b]*Institute for Superconducting and Electronic Materials, University of Wollongong, Innovation Campus, Squires Way, North Wollongong, NSW 2500, Australia. E-mail: cheng@uow.edu.au*

[c]*Guangxi Key Laboratory of Processing for Non-Ferrous Metals and Featured Materials, Key Laboratory of New Processing Technology for Non-Ferrous Metals and Materials, Ministry of Education, School of Resources, Environment and Materials, Guangxi University, Nanning, 530004, China*

† Electronic supplementary information (ESI) available. See DOI: 10.1039/d0ra10807c

nanoferroelectric materials can absorb versatile environmental energy, such as solar energy, mechanical energy, and heat, to degrade dyes in a specific way.

As a common class of ferroelectric materials, the chemical formula of the tungsten bronze structure can be described as $(A1)_2(A2)_4(C)_4(B1)_2(B2)_8O_{30}$. In a unit cell of the tetragonal system, the structure is connected by the vertices of the oxygen octahedral unit, forming two tetra-atomic rings (A1), four five-membered rings (A2), and four triatomic rings (C). If one of the A sites is empty, it becomes an unfilled tungsten bronze structure with the formula $A_5B_{10}O_{30}$.[16] The ions in the center of the oxygen octahedron and the ions in the gap position (mainly the A site) are displaced along the *c*-axis direction, forming a non-central symmetric structure with an electric dipole moment along the *c*-axis, which is also a tungsten bronze crystal ferroelectric source.[17–20] In recent years, due to the excellent ferroelectric, piezoelectric, pyroelectric, and nonlinear optical properties of tungsten bronze materials,[21,22] they have gradually attracted widespread attention. In addition, the ferroelectric polarization of the tungsten bronze compound helps guide the migration of carriers, often playing an important role in the catalytic process.[23–25] Recently, Zhang *et al.*[26] reported that platinum nanoparticles supported on defective tungsten bronze $KSr_2Nb_5O_{15}$ can work as a new type of photocatalyst for efficient ethylene oxidation. Takayama *et al.*[27] reported a tungsten bronze structure $KCaSrTa_5O_{15}$ photocatalyst for water splitting and CO_2 reduction. These works all indicate that tungsten bronze structural compounds have great potential in the field of catalysis.

We have developed a tungsten bronze structure $Ba_4Nd_2Fe_2Nb_8O_{30}$ (BNFN) for efficient degradation of dyes under friction.[28] On this basis, we further explore the mechanism of tribocatalysis. Taking into account the high photocatalytic activity of tantalum-based photocatalysis, which is mainly due to their high conduction bands formed by Ta 5d orbitals.[27] We choose another unfilled tungsten bronze structure, $Ba_{2.5}Sr_{2.5}Nb_8Ta_2O_{30}$ (BSNT) usually has a large number of oxygen vacancies and a larger movable charge density (holes),[18,19] which results in relatively better electrical conductivity (compared to $Ba_{0.75}Sr_{0.25}TiO_3$ perovskites). In such a ferroelectric material with a large amount of internal movable charges, the shielding of the depolarization field should come from its own internal charges (and not the adsorbed space charged particles, such as $LiNbO_3$).[14] When contacting other materials with different polarities, the shielding internal charges accumulated at the submicron particle surface are prone to transfer between the different materials. After the charge is transferred to contacting materials, the internal electric field of the ferroelectric particle is instantly imbalanced (non-zero), which further promotes the separation and movement of the internal electrons and holes. Therefore, BSNT with simultaneous polarization and many charge carriers may outperform other ferroelectric materials that have very limited movable charges, benefiting from fast charge transfer during friction and therefore better catalytic degradation.

In this study, we synthesized tungsten bronze-type $Ba_{2.5}Sr_{2.5}Nb_8Ta_2O_{30}$ by a high-temperature solid-phase reaction and obtained submicron-sized powder by high-energy ball milling. BSNT submicron particles can induce the degradation of dye in a water suspension under magnetic stirring in the dark at room temperature. By optimizing the experimental conditions, rhodamine B (RhB) can be degraded with an efficiency of up to 99%. The driving force for decomposing the dye is mainly the tribocatalytic effect of the friction between the BSNT submicron particles and PTFE stirring rod and the beaker rather than the piezocatalytic effect. Charge transfer between ferroelectric BSNT and PTFE rods or beakers during friction leads to an unbalanced internal electric field in BSNT particles to drive fast electron–hole separation and the creation of $^{\bullet}OH$ and $^{\bullet}O_2^-$, resulting in even higher efficiency dye degradation than the piezocatalytic effect. This work reveals that friction mechanical energy in a system with the involvement of ferroelectric materials can efficiently drive catalytic degradation, paving the way for environmental remediation by versatile materials using the trivial mechanical energy of the environment.

2. Experimental procedures

2.1 Synthesis of $Ba_{2.5}Sr_{2.5}Nb_8Ta_2O_{30}$ submicron particles

Powders of $Ba_{2.5}Sr_{2.5}Nb_8Ta_2O_{30}$ were prepared by a solid-state reaction. $BaCO_3$ (99.99%, Aladdin), $SrCO_3$ (99.99%, Aladdin), Nb_2O_5 (99.99%, Sinopharm), and Ta_2O_5 (99.99%, Sinopharm) were used as starting materials. In accordance with the molar ratio of $BaCO_3 : SrCO_3 : Nb_2O_5 : Ta_2O_5 = 5 : 5 : 8 : 2$, anhydrous ethanol was used as a ball mill medium after being ground for 12 h, dried and compressed into a pellet, and calcined in air at 1200 °C for 4 h. Thereafter, the prepared pre-sintered pellets were subjected to secondary ball milling, and then the dried powders were recompressed into a pellet and sintered at 1400 °C for 6 hours in the air atmosphere of a high-temperature furnace. Finally, the sintered samples were placed in a high-energy ball mill machine (Pulverisette 5, Fritsch), ground at 300 rpm for 24 hours using anhydrous ethanol as a ball mill medium, and dried at 120 °C for 4 h to obtain $Ba_{2.5}Sr_{2.5}Nb_8Ta_2O_{30}$ submicron powders.

2.2 BSNT ferroelectric performance test

A high-temperature solid-phase method was used to synthesize a 1 mm thick BSNT ceramic wafer at 1400 °C, and then silver paste was applied on both sides of the wafer. The silver electrode was fired at 650 °C for 30 minutes, and then the room-temperature *P–E* hysteresis loop was measured using a Radiant Precision 10 kV HVI-SC analyzer at 2700 V and 1 Hz. The room temperature impedance analysis was measured using an Agilent 4294A precision impedance analyzer.

2.3 Characterization

The crystal structures of the BSNT powders were characterized by X-ray diffraction (XRD, PANalytical X'Pert PRO, Netherlands) at ambient temperature using Cu Ka radiation ($\lambda = 0.15406$ nm). Elemental analysis and content determination of BSNT submicron particles were performed by energy dispersive X-ray spectrometry (EDS, Horiba X-Max). The surface morphologies and nanoscale microstructures of the prepared BSNT

submicron powders were examined by field emission scanning electron microscopy (FESEM, Hitachi S-4800), transmission electron microscopy (TEM, JEOL JEM-2100F) and high-resolution transmission electron microscopy (HRTEM) combined with selected area electron diffraction (SAED) patterns. Atomic force microscopy (AFM, NT-MDT) was used to describe the morphology of BSNT submicron particles. The particle size distribution of BSNT was characterized using a Zetasizer (Malvern Zetasizer Nano S90, UK). The elemental composition and valences of the BSNT sample were determined by X-ray photoelectron spectroscopy (XPS, Thermo Fisher ESCALAB 250Xi) with Al Ka X-ray as the excitation source.

2.4 Dye degradation test

The catalytic capability of BSNT submicron particles was demonstrated by the degradation of RhB. In this experiment, 50 mg of BSNT submicron powder was added to a glass beaker (Ø 51 mm × 70 mm), followed by 50 mL of RhB solution (5 mg L^{-1}) and a polytetrafluoroethylene (PTFE) magnetic rod (specification Ø 9 mm × 25 mm). The glass container was placed in the middle of a magnetic stirrer, and stirring was carried out at room temperature in the dark with a rotation speed of 300 rpm. Three milliliters of supernatant liquor was removed from the beaker at regular intervals. After the high-speed centrifugation of the sample suspension liquid, the absorbance of the liquid sample was measured using an ultraviolet-visible spectrophotometer (UV-3600; Shimadzu, Kyoto, Japan). For the recycling test, 50 mg of BSNT submicron powder was put into 50 mL of RhB (5 mg L^{-1}) solution, magnetically stirred by three PTFE stirring rods for 2 h, centrifuged, washed with deionized water, dried and recycled.

2.5 Detection of active species

Electron spin resonance (ESR) is widely used to detect active free radicals. The spin-trap molecules react with free radicals to produce stable products in solution, which can be directly detected by ESR.[29–31] The main active substances in the dye degradation process are $^{\cdot}OH$ and $^{\cdot}O_2^-$, which can be detected using ESR technology. The specific detection process was to add 50 mg of BSNT submicron particles to 50 mL of DI water and 50 mL of dimethyl sulfoxide (DMSO). Next, 5,5-dimethyl-1-pyrroline *N*-oxide (DMPO) was used as a spin trap in DI water and DMSO. Both suspensions were magnetically stirred with three PTFE rods at 300 rpm at room temperature in the dark. After different stirring times, the ESR signal spectrum of the spin-trapped free radicals was measured and recorded with an ESR spectrometer (JES-FA200, JEOL).

To further study the friction catalysis mechanism of BSNT, free radical trapping and hole trapping experiments were carried out to determine the main active substances in the friction catalysis process. Before stirring, 1 mM tert-butanol (TBA, a scavenger of hydroxyl radicals),[32] *p*-benzoquinone (BQ, a scavenger of superoxide radicals)[33] and ethylenediaminetetraacetic acid (EDTA, a scavenger of holes)[34] were added to three glass beakers containing 50 mL of RhB (5 mg L^{-1}) and 50 mg of a BSNT submicron powder suspension. Subsequently, magnetic stirring was performed at 300 rpm using three PTFE stirring rods in the dark at room temperature. After centrifugation of the removed 3 mL of supernatant at different intervals, the degradation rate of RhB in the solution was measured with a Shimadzu UV-3600.

3. Results and discussion

3.1 Structural characterizations

Fig. 1a shows the XRD pattern of $Ba_{2.5}Sr_{2.5}Nb_8Ta_2O_{30}$ of the as-sintered and ball milled samples. All samples are pure tetragonal tungsten-bronze phase with the *P4bm* space group, according to diffraction peaks indexed using the PDF2 card no. 00-039-0265. After high-energy ball milling, the BSNT powder was reduced to the submicron level, which is reflected by the decreased intensity and increased FWHM of the diffraction peaks. Fig. 1b shows the polarization-electric field (*P*–*E*) curve of the BSNT ceramic at room temperature, confirming the ferroelectricity of BSNT. The residual polarization (P_r) of the BSNT ceramic is 1.01 μC cm^{-2}. Fig. S1† shows the EDS result of BSNT. The element mapping of the constituent elements Ba, Sr, Nb, Ta, and O are uniformly distributed, which are consistent with the BSNT particles. The particle morphology and size distribution of ball-milled BSNT shows sizes ranging from 10 nm to 400 nm, and Zetasizer shows that the average particle size of the particles is 170 nm (Fig. 1c and d). Atomic Force Microscopy (AFM) was used to characterize the thickness of BSNT submicron particles. BSNT submicron particles are clearly observed in the AFM image (Fig. S2a†). Fig. S2b† is the outline of the line

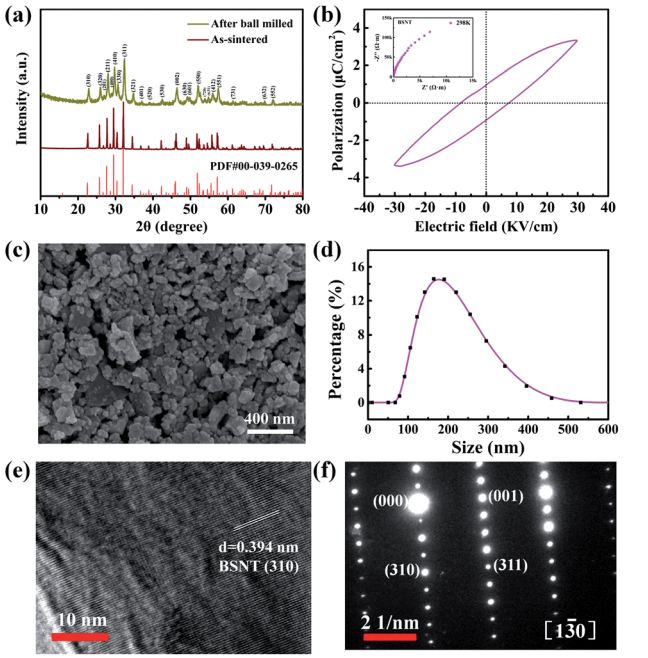

Fig. 1 (a) XRD pattern, (b) room temperature *P*–*E* at 2700 V and 1 Hz of BSNT, (c) SEM photograph, and (d) size distribution of BSNT submicron particles. (e) High-resolution pattern and (f) selected electron diffraction of BSNT submicron particles. The inset of (b) shows impedance of BSNT at room temperature.

along the purple line in the AFM image, indicating that the thickness of the BSNT submicron particles is about 175 nm. The HRTEM results are shown in Fig. 1e. BSNT submicron particles have a single crystal structure with a lattice spacing of 0.394 nm, corresponding to the (310) plane in the BSNT tetragonal tungsten bronze structure. Fig. 1f is the selected area electron diffraction (SAED) pattern along the [130] TTB band axis at room temperature. The essential reflections in the pattern can be indexed on the tetragonal cell *P4bm*, with cell parameters of $a_{TTB} = b_{TTB} \approx 12.5$ Å and $c_{TTB} \approx 4$ Å.

3.2 Surface element analysis

X-ray photoelectron spectroscopy (XPS) was used to identify the powder chemical components and the valence states of the constituent elements. Fig. 2a is the full spectrum of BSNT submicron particles in the range of 1000–0 eV binding energy. The binding energies of Ba, O, Nb, Sr, and Ta were calibrated with the binding energies of C 1s. Detailed XPS modes from high energy to low energy of each element are shown in Fig. 2b–f. Gaussian fitting was used to split overlapping peaks into different parts. Fig. 2b of the Ba 3d spectrum shows two symmetrical peaks at 794.8 eV and 779.5 eV, corresponding to Ba $3d_{3/2}$ and Ba $3d_{5/2}$, respectively, indicating that Ba^{2+} ions were present in the sample.[13] Fig. 2c shows that the asymmetric O 1s peak is fitted by two peaks, numbered 1 and 2. Peak 1 is attributed to the lattice oxygen in the tungsten bronze structure, while the additional peak 2 may be caused by the chemical adsorption of the oxygen group at the oxygen vacancy or the presence of an OH group on the surface.[35,36] Fig. 2d shows the double peaks of Nb $3d_{3/2}$ and $3d_{5/2}$ with binding energies at 209.4 eV and 206.7 eV, respectively. The spin–orbit peak separation energy is 2.7 eV, confirming the presence of Nb^{5+} ions.[35] Both Sr $3d_{3/2}$ and Sr $3d_{5/2}$ can be well fitted by two peaks with binding energies at 134.9 eV and 133.2 eV (Fig. 2e), giving the sign of Sr^{2+} ions.[35] In Fig. 2f, Ta 4f fits into two subpeaks of Ta $4f_{5/2}$ (27.4 eV) and Ta $4f_{7/2}$ (25.5 eV), which are characteristic peaks of Ta^{5+} in compounds.[36]

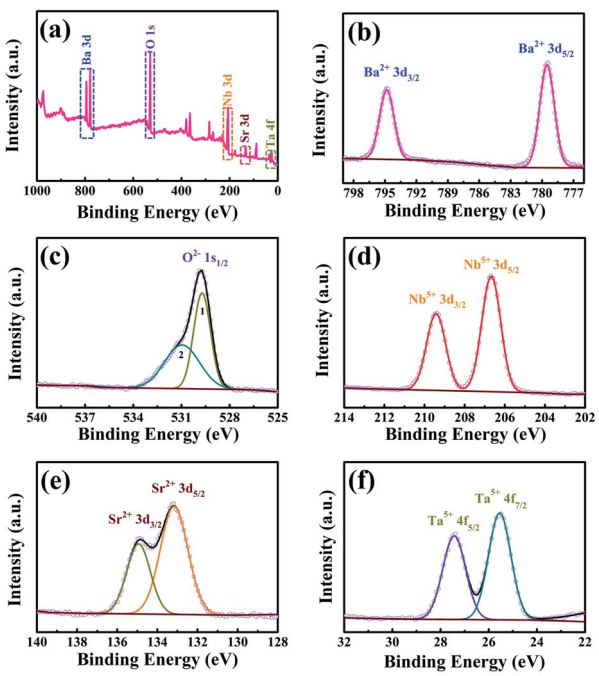

Fig. 2 (a) XPS survey scan of the BSNT submicron particles. (b) XPS core level spectra of Ba 3d. (c) XPS core level spectra of O 1s. (d) XPS core level spectra of Nb 3d. (e) XPS core level spectra of Sr 3d. (f) XPS core level spectra of Ta 4f.

3.3 Tribocatalytic activity

To study the catalytic properties of the as-prepared BSNT submicron powders, RhB dye was selected for the degradation experiment. As shown in Fig. 3a, the color of the solution gradually became lighter during magnetic stirring at 300 rpm of the BSNT submicron powder RhB dye suspension (as shown in the illustration) using one PTFE stirring rod and glass beaker at room temperature in the dark. Simultaneously, the maximum absorption peak intensity of the UV-visible absorption spectrum at ~554 nm gradually weakens with increasing stirring time. Generally, the intensity of maximum absorbance is closely related to the concentration of dye, according to the Lambert–Beer law formula:

$$A = \varepsilon \times b \times c \quad (1)$$

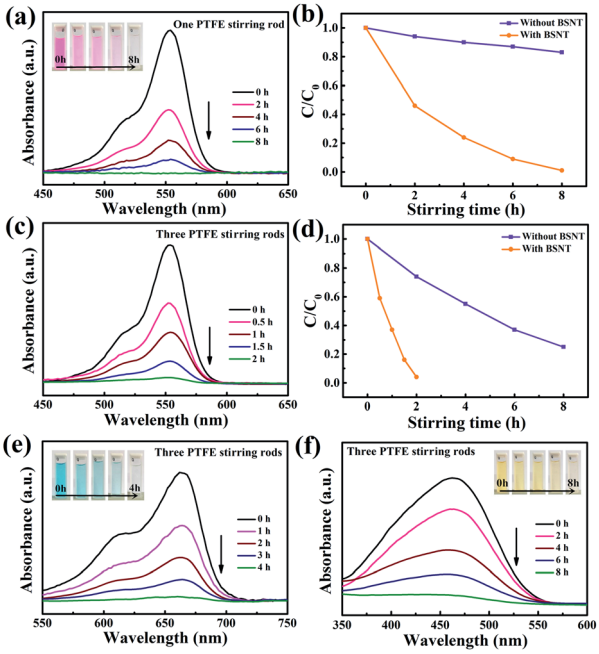

Fig. 3 (a) and (c) UV-vis adsorption spectra of RhB solution mediated by BSNT submicron particles under magnetic stirring with one PTFE rod and three PTFE rods in the dark at room temperature, respectively. (b) and (d) The tribocatalytic RhB dye degradation efficiency after different magnetic stirring with or without BSNT, using one PTFE stirring rod and three PTFE stirring rods, respectively. (e) and (f) UV-vis adsorption spectra of MB and MO solutions mediated by BSNT submicron particles under magnetic stirring with three PTFE rods in the dark at room temperature, respectively. The insets of (a), (e), and (f) show the color changes of the RhB, MB and MO solutions, respectively.

where A is the absorbance, ε is the molar absorption coefficient, b is the path length through the sample, and c is the concentration of the test dye solution. Moreover, the degradation efficiency (D) of the dye can be calculated based on the following equation:

$$D = (1 - A/A_0) \times 100\% \quad (2)$$

where A_0 and A represent the initial absorption of the dye solution and actual absorption peak intensity after degradation, respectively. The degradation efficiency of RhB dye increases rapidly with increasing stirring time, reaching 99% after 8 h of magnetic stirring, as shown in Fig. 3b. To further confirm the role of BSNT submicron powders in the catalytic process, control experiments were conducted. As shown in Fig. 3b, in the RhB degradation experiment without the addition of BSNT submicron powders, the dye can be slightly degraded by friction agitation between the PTFE rod and glass beaker alone. In contrast, adding BSNT submicron powders can greatly improve the degradation rates of dyes.

In a typical experiment, we used three PTFE stir bars for stirring the RhB-BSNT suspension at 300 rpm in a glass beaker at room temperature in the dark to further improve the catalytic degradation rate of RhB dye by BSNT submicron powders. It is clearly shown from Fig. 3c and d that the degradation rate is much faster than that of one stirring rod with a degradation efficiency up to 96% after stirring for 2 h when three PTFE stirring rods were used. It is worth noting that when BSNT submicron powders are not added, the RhB decomposition rate of three rods stirring is also much higher than that of one rod stirring but much less than the case with BSNT powders. Therefore, the significant increase in the decomposition rate is related to the increased contact area between the three magnetic stirring rods and the glass and between the stirring rods and BSNT particles.

To further verify the degradation effect of the designed system, other pollutants, such as methylene blue (MB) and methyl orange (MO), were also used. The results are shown in Fig. 3e and f. At room temperature, in the dark, using three PTFE stirring rods in a glass beaker at a speed of 300 rpm stirring MB–BSNT, the MO–BSNT suspension also showed similar results. The degradation efficiency of MB is 98.5% after 4 h of stirring, which is 91% after 8 h of stirring for MO solution. The variation in degradation efficiency for the three types of dyes is associated with the different molecular structures and corresponding different degradation mechanisms.[37,38] The results show that the strong frictional catalytic activity of the BSNT submicron particles significantly accelerates the de-ethylation process of RhB and eventually forms a completely de-ethylated product.[39] Compared with MB and RhB, the activity of the N=N double bond is much lower in MO, which makes it more difficult to degrade.[40]

In another experiment, we studied the degradation experiments of the friction between PTFE and glass, where two different types of magnetic stirring glass and PTFE rods and beakers made of glass, PTFE and polypropylene (PP) were used. Fig. 4a and b shows the degradation rate of RhB dye (a) without BSNT and (b) with BSNT after different stirring times when using three stirring rods at the same speed of 300 rpm in the dark. The results show that the friction between the different materials leads to a large difference in the RhB decomposition rate. As shown in Fig. 4a, when BSNT submicron powder is not added, in the cases with glass rods–PP beaker, PTFE rods–PTFE beaker, PTFE rods–glass beaker, glass rods–PTFE beaker, PTFE rods–PP beaker, glass rods–glass beaker, after stirring for 2 h, the degradation rates of RhB are 64%, 46%, 33%, 26%, 22% and 2%, respectively. As shown in Fig. 4b, after adding BSNT submicron powders, except for the glass rods–glass beaker system, the degradation efficiencies of RhB increase significantly. Rather surprisingly, when BSNT submicron powders were added to the glass rods–PP beaker system and stirred for only 1.5 h, a degradation efficiency of 99% was achieved. In contrast, despite stirring at the same speed, the catalytic degradation rate of the glass rods–glass beaker system with BNST powders was only 6% in 2 h. The above results indicate that the degradation of RhB dye in the presence of BSNT powders is not the simple physical adsorption of dye by BSNT submicron particles.

Subsequently, in the glass beaker–PTFE rods system, we selected the non-ferroelectric raw material Ta_2O_5 submicron particles used to synthesize BSNT for comparative experiments. The results are shown in Fig. 4c. RhB degraded slowly after stirring for two hours on three PTFE rods. In sharp contrast with BSNT submicron particles.

To evaluate the stability and recyclability of BSNT particles in the catalysis process, a recycling test was conducted on the tribocatalytic ability of BSNT submicron particles. Then, 50 mg of BSNT submicron powder was put into 50 mL of RhB (5 mg L^{-1}) solution and magnetically stirred by three PTFE stirring rods for 2 h, centrifuged, washed with deionized water,

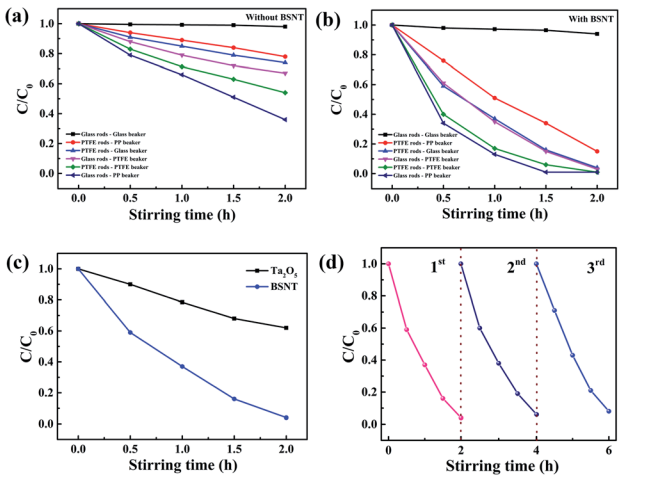

Fig. 4 The dye degradation efficiency for RhB dye (a) without BSNT and (b) with BSNT submicron particles under magnetic stirring in the dark at room temperature with different stirring rods and beakers. (c) The degradation efficiency of BSNT and Ta_2O_5 submicron particles on RhB dye under room temperature dark magnetic stirring conditions. (d) Recycling stability of BSNT submicron particles for RhB degradation.

dried and recycled. As shown in Fig. 4d, after three cycles of use, the BSNT catalytic efficiency can still reach more than 92%. The XRD test was performed on the BSNT sub-micron particles after the degradation test. As shown in Fig. S3,† the XRD spectra of the BSNT sub-micron particles before and after the tribocatalysis were very similar, and no secondary phase was found, indicating that the BSNT catalyst has good stability and recyclability, which is conducive to its long-term use in the degradation of organic pollutants.

3.4 Mechanism of tribocatalytic activity

The above results reveal the critical role played by BSNT particles in the friction degradation of dyes. As a catalyst, the catalytic behavior of BSNT is determined by its electronic structure. The electronic structure of BSNT can be obtained through ultraviolet-visible spectroscopy and XPS spectroscopy. Fig. 5a shows the UV-vis absorption spectra of BSNT, and Fig. 5b shows the band gap, E_g, derived from the formula $(\alpha h\nu)^{1/2} = A(h\nu - E_g)$[41] with a value of 3.86 eV. Fig. 5c shows that the value of the valence band can be evaluated based on the XPS binding energy with a value of 1.96 eV. The valence band (VB), conduction band (CB) of BSNT and the potential of $OH^-/{}^{\bullet}OH$ and $O_2/{}^{\bullet}O_2^-$ are shown in Fig. 5d. The hole on the VB of BSNT can react with OH^- to form hydroxyl radicals ($^{\bullet}OH$) because $OH^-/{}^{\bullet}OH$ is less than positive than the VB, while $O_2/{}^{\bullet}O_2^-$ is less negative than the CB of BSNT, indicating that the electrons in the CB can cause absorbed O_2 to form superoxide radical anions ($^{\bullet}O_2^-$).[41,42] This result indicates that the band structure of BSNT meets the requirement for the generation of active radicals for dye degradation.

With meeting the band requirement, how BSNT submicron particles accelerate the degradation of dyes and what the driving force of the catalytic behavior is remain open questions. Based on the above measurements and control experiments, the dye degradations observed can undoubtedly be categorized as tribocatalytic reactions. Taking the PTFE rod–glass beaker system as an example, as shown in Fig. 6a, it can be inferred that the dye degradation by friction between the stirring rods and beakers of different materials can be attributed to triboelectric charging.[43] Due to the significant difference in the electron affinity of the PTFE stirring rods and glass beaker, electrons are transferred from the glass to the surface of the PTFE during frication, and the induced charges on the polymer surface will react with the water and oxygen in the dye solution to form hydroxyl radicals ($^{\bullet}OH$) and superoxide radical anions ($^{\bullet}O_2^-$) and participate in dye degradation.[44] When the magnetic stirring stops, the generated triboelectric charges will also be consumed, and the surface will be neutralized. As shown in Fig. 4a, the degradation efficiency of the glass rods–glass beaker system is very low. It is generally believed that, for weakly polar materials such as glass, the same material during friction has the same ability to bond extranuclear electrons, and it is unlikely to transfer electrons. Therefore, triboelectricity in such a system should be ignored. However, it is worth noting that, in the PTFE rods–PTFE beaker system, the degradation efficiency of RhB is much higher than that of the glass–glass system. This seems to break the common rule of triboelectricity, but it reflects the influence of hidden coupling factors. The asymmetric contact theory can explain this phenomenon.[45] For example, when two identical polymers (such as PTFE) are rubbed or squeezed, they may cause nanoscale damage/fracture and possibly material transfer, that is, deep material exchange. In addition, even two identical polymer materials can have different exposed surface layer compositions and varied atom compositions at different depths, which can cause charge

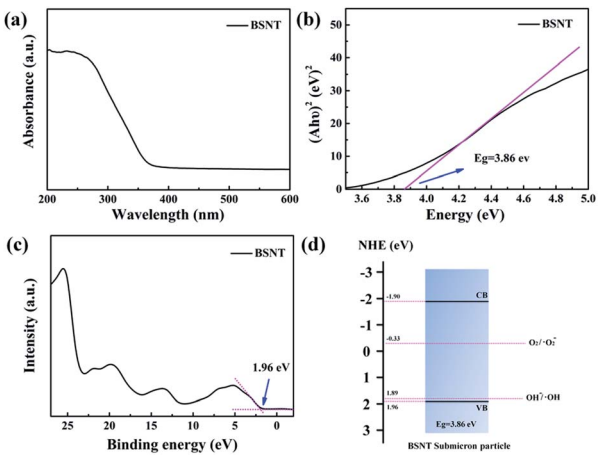

Fig. 5 (a) UV-vis absorption spectra, (b) plots of $(\alpha h\nu)^{1/2}$ *vs.* photon energy, (c) total density states of the XPS valence band of BSNT, and (d) comparison diagram of the VB, CB and potentials of $^{\bullet}OH$ and $^{\bullet}O_2^-$.

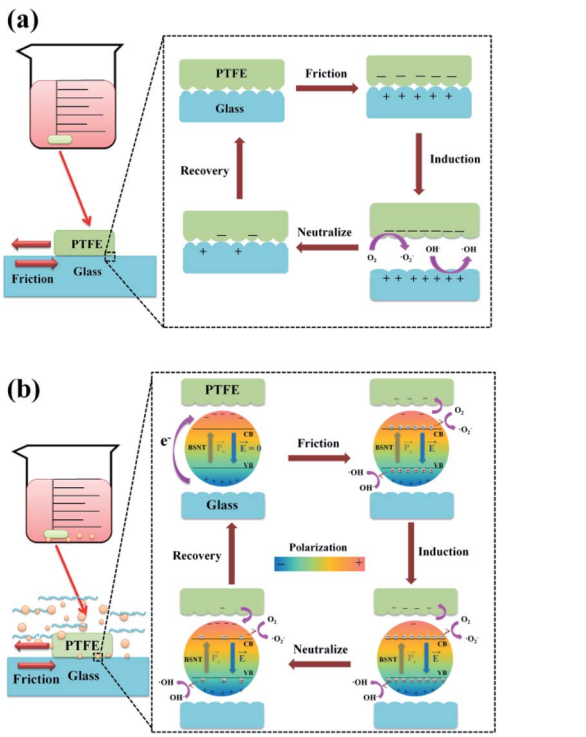

Fig. 6 Schematic diagram of the tribocatalytic process with the involvement of ferroelectric materials, (a) without BSNT particles, (b) with BSNT submicron particles.

transfer at the point of contact.[46] This can explain why even two identical polymer materials can be triboelectrically charged with friction.

With the addition of BSNT particles, the degradation efficiency increases significantly, which is inseparable from the fact that BSNT submicron particles can catalyze the chemical reaction driven by the mechanical friction energy. As shown in Fig. 6b, in the process, the structure of the BSNT unit cell makes the positive and negative charge centers do not coincide and an electric dipole moment appears, resulting in an electric polarization intensity that is not equal to zero, so that the crystal has spontaneous polarization. At this time, the internal electrons or holes will be driven to the particle surface to shield the polarization field, leading to a zero net electric field entirety the material at the equilibrium state. At the beginning of friction, due to the difference in electronegativity between PTFE and BSNT, the strong electrostatic attraction generated by friction causes electron transfer from the BSNT surface to the surface of PTFE, causing a non-zero internal electric field in BNST particles. It is noteworthy that the accumulated charges on the ferroelectric BSNT surface will facilitate the charge transfer process. Driven by the internal electric field, electrons in the valence band (VB) are excited to transition to the conduction band (CB) and then move to the particle surface, and the remaining holes will move to the opposite end of the particle surface, which in turn induces a series of redox reactions in dye degradation on the surface of the BSNT particles as follows:

$$\mathrm{BSNT} \xrightarrow{\text{triboelectric energy}} \mathrm{BSNT} + h^{+}_{VB} + e^{-}_{CB} \quad (3)$$

$$OH^{-} + h^{+}_{VB} \rightarrow {}^{\bullet}OH \quad (4)$$

$$O_2 + e^{-}_{CB} \rightarrow {}^{\bullet}O_2^{-} \quad (5)$$

$$\mathrm{Dye} + {}^{\bullet}OH\ ({}^{\bullet}O_2^{-}) \rightarrow \mathrm{degradation} \quad (6)$$

where e^{-}_{CB} represents electrons excited to the conduction band (CB), and h^{+}_{VB}. h^{+}_{VB} represents holes formed in the valence band (VB). It is important to point out that when BSNT submicron powders are added to the glass rods–glass beaker system for stirring, almost no degradation of RhB dye is observed. This can be explained from the perspective of charge transfer between different friction materials. Since glass and BSNT particles are both weakly polar materials and do not contain atoms with high electron affinity, electron transfer does not easily occur during friction, and there is no apparent breaking of the established internal electric field balance needed for driving the separation of electron–hole pairs. For other systems, the BSNT particles must be rubbed with other materials to produce enough triboelectric charge to induce a large enough internal electric field to drive the separation of electron–hole pairs. It is worth noting here that the internal polarization of the BSNT has remained unchanged in the friction process, so the internal stable polarization becomes the driving force for the surface charge to restore the charge balance after the two materials are separated from the friction. This advantage is not observed for non-ferroelectric materials.

To explore the active species produced in the tribocatalytic process, ESR was used to observe ${}^{\bullet}OH$ and ${}^{\bullet}O_2^{-}$ radicals. Fig. 7a shows the DMPO–${}^{\bullet}OH$ spectra of the solution with different stirring times. The figure shows that four characteristic peaks (1 : 2 : 2 : 1) appeared after stirring for 1 h and 2 h, but no ESR signal was observed without stirring.[47,48] Similarly, as shown in Fig. 7b, the DMPO–${}^{\bullet}O_2^{-}$ signal spectrum was observed in the BSNT–DMSO suspension with magnetic stirring.[49,50] Both ${}^{\bullet}OH$ and ${}^{\bullet}O_2^{-}$ free radicals were detected, which provides evidence for electron–hole pair creation and separation by friction between BSNT submicron particles and PTFE.

In order to monitor the intermediate products of the tribocatalytic process, TA was used as a probe molecule to observe ${}^{\bullet}OH$ radicals.[4] Fig. S4† shows the dependence of the fluorescence intensity of 2-hydroxyterephthalic acid (${}^{\bullet}OH$ capture) on the friction stirring time at the PL excitation wavelength of 315 nm. With the increase of the stirring time, the intensity of the fluorescence emission peak gradually increased at 425 nm, indicating that ${}^{\bullet}OH$ radicals were stably generated. It also supports the generation of triboelectrically induced charges during tribocatalysis.

To further reveal the effect of free radicals generated during friction on the degradation of dyes, as shown in Fig. 7c, the addition of TBA significantly inhibited the degradation, indicating that ${}^{\bullet}OH$ plays an important role in the observed dye degradation. On the other hand, after the addition of BQ, the degradation of RhB is slightly reduced, and the addition of EDTA has little effect on the degradation of RhB, indicating that the hole is not the main active substance during the degradation process.

In this experiment, according to the first and second laws of thermodynamics, the heat generated by friction is consumed by the vaporization of the dye solution.[51] The temperature of the reaction solution is near room temperature, and it is impossible

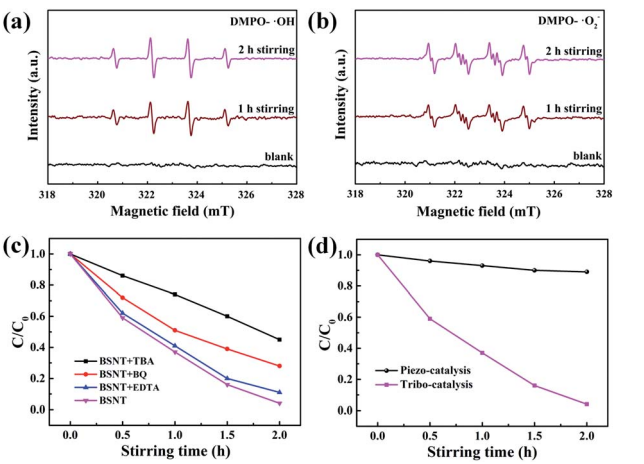

Fig. 7 The DMPO spin-trapping ESR spectra of BSNT submicron powders in (a) a H_2O dispersion for DMPO–${}^{\bullet}OH$ and (b) a DMSO dispersion for DMPO–${}^{\bullet}O_2^{-}$. (c) Effects of adding different radical scavengers on the tribocatalytic RhB dye degradation mediated by BSNT. (d) The degradation efficiencies of RhB with different catalytic methods at 2 h.

to cause the degradation of the observed dye, so the friction heat effect is negligible. In addition, the possibility that the magnetic field applied by the magnetic stirrer is the driving force for degrading the dye can be ruled out because the friction between the stirring rods and beakers of different materials can result in a significant difference in the efficiency of degrading the dye under the same magnetic field conditions. It is also worth noting that the BSNT catalyst is a ferroelectric material that can exhibit a piezoelectric effect for the piezocatalytic effect. However, piezoelectric catalysis usually occurs under high-frequency ultrasonic vibration,[52–54] and the macroscopic vibration caused by low frequency friction does not easily bend the submicron particles for piezocatalysis. Then, another experiment was carried out to check the ultrasonic (40 kHz) vibration degradation of the RhB dye by BSNT submicron particles. As shown in Fig. 7d, the results show that there was no obvious degradation of RhB in a solution containing BSNT particles under ultrasonic vibration, which further confirmed that the contribution of piezoelectric catalysis in this experiment was negligible.

4. Conclusions

In summary, the mutual friction of the polymers can induce the degradation of the dye at room temperature in the dark. After adding BSNT submicron powder, the dye degradation efficiency greatly improved. When three glass stirring rods were used in the PP beaker and the BSNT–RhB suspension was stirred at 300 rpm, the RhB degradation efficiency was further improved to 99% within 1.5 h. The observed $^{\bullet}OH$ and $^{\bullet}O_2^-$ intermediates with strong oxidizing ability indicate that the strong spontaneous polarization of ferroelectric BSNT submicron particles can benefit the separation of internal electron and hole pairs under mechanical friction with other materials. Our work clearly shows that ferroelectric materials, such as BSNT submicron particles, can be driven by trivial mechanical energy from the environment for dye degradation, which could be found to be important for applications in environmental remediation. These results fully show that there is great potential in collecting friction energy for environmental governance.

Conflicts of interest

There are no conflicts to declare.

Acknowledgements

All the authors thank the National Natural Science Foundation of China (11564009), Natural Science Foundation of Guangxi (2018GXNSFAA050010, 2019GXNSFGA245006), high level innovation team and outstanding scholar program of Guangxi institutes, and open founding of the Key Laboratory of New Processing Technology for Nonferrous Metal & Materials, Ministry of Education/Guangxi Key Laboratory of Optical and Electronic Materials and Devices (19AA-15, 20KF-16) for financial support.

References

1 H. L. You, Y. M. Jia, Z. Wu, X. L. Xu, W. Q. Qian, Y. T. Xia and M. Ismail, Strong piezo-electrochemical effect of multiferroic $BiFeO_3$ square micro-sheets for mechanocatalysis, *Electrochem. Commun.*, 2017, **79**, 55–58.

2 S. Mosleh, K. Dashtian, M. Ghaedi and M. Amiri, A Bi_2WO_6/Ag_2S/ZnS Z-scheme heterojunction photocatalyst with enhanced visible-light photoactivity towards the degradation of multiple dye pollutants, *RSC Adv.*, 2019, **9**, 30100–30111.

3 J. Y. Zhang, C. L. Su, X. J. Xie, P. Liu and M. E. Huq, Enhanced visible light photocatalytic degradation of dyes in aqueous solution activated by HKUST-1: performance and mechanism, *RSC Adv.*, 2020, **10**, 37028–37034.

4 X. L. Xu, S. J. Chen, Z. Wu, Y. M. Jia, L. B. Xiao and Y. S. Liu, Strong pyro-electro-chemical coupling of $Ba_{0.7}Sr_{0.3}TiO_3$@Ag pyroelectric nanoparticles for room-temperature pyrocatalysis, *Nano Energy*, 2018, **50**, 581–588.

5 A. Kakekhani and I. Sohrab, Polarization-driven catalysis via ferroelectric oxide surfaces, *Phys. Chem. Chem. Phys.*, 2016, **18**, 19676–19695.

6 H. L. You, X. X. Ma, Z. Wu, L. F. Fei, X. Q. Chen, J. Yang, Y. S. Liu, Y. M. Jia, H. M. Li, F. F. Wang and H. T. Huang, Piezoelectrically/pyroelectrically-driven vibration/cold–hot energy harvesting for mechano-/pyro-bi-catalytic dye decomposition of $NaNbO_3$ nanofibers, *Nano Energy*, 2018, **52**, 351–359.

7 E. K. Akdogan, C. J. Rawn, W. D. Porter, E. A. Payzant and A. Safari, Size effects in $PbTiO_3$ nanocrystals: effect of particle size on spontaneous polarization and strains, *J. Appl. Phys.*, 2005, **97**, 084305.

8 J. Wu, N. Qin, B. W. Yuan, E. Z. Lin and D. H. Bao, Enhanced pyroelectric catalysis of $BaTiO_3$ nanowires for utilizing waste heat in pollution treatment, *ACS Appl. Mater. Interfaces*, 2018, **10**, 37963–37973.

9 A. Al-keisy, L. Ren, D. D. Cui, Z. F. Xu, X. Xu, X. D. Su, W. C. Hao, S. X. Dou and Y. Du, A ferroelectric photocatalyst $Ag_{10}Si_4O_{13}$ with visible-light photooxidation properties, *J. Mater. Chem. A*, 2016, **4**, 10992–10999.

10 Q. Fu, X. J. Wang, C. Y. Li, Y. Sui, Y. P. Han, Z. Lv, B. Song and P. Xu, Enhanced photocatalytic activity on polarized ferroelectric $KNbO_3$, *RSC Adv.*, 2016, **6**, 108883–108887.

11 X. R. Xiong, R. M. Tian, X. Lin, D. W. Chu and S. Li, Formation and photocatalytic activity of $BaTiO_3$ nanocubes via hydrothermal process, *J. Nanomater.*, 2015, **2015**, 692182.

12 S. S. Wang, Z. Wu, J. Chen, J. P. Ma, J. S. Ying, S. C. Cui, S. G. Yu, Y. M. Hu, J. H. Zhao and Y. M. Jia, Lead-free sodium niobate nanowires with strong piezo-catalysis for dye wastewater degradation, *Ceram. Int.*, 2019, **45**, 11703–11708.

13 X. L. Xu, L. B. Xiao, Y. M. Jia, Z. Wu, F. F. Wang, Y. J. Wang, N. O. Haugen and H. T. Huang, Pyro-catalytic hydrogen evolution by $Ba_{0.7}Sr_{0.3}TiO_3$ nanoparticles: harvesting cold–hot alternation energy near room-temperature, *Energy Environ. Sci.*, 2018, **11**, 2198–2207.

14 E. Gutmann, A. Benke, K. Gerth, H. Bottcher, E. Mehner, C. Klein, U. Krause-Buchholz, U. Bergmann, W. Pompe

and D. C. Meyer, Pyroelectrocatalytic disinfection using the pyroelectric effect of nano- and microcrystalline $LiNbO_3$ and $LiTaO_3$ particles, *J. Phys. Chem. C*, 2012, **116**, 5383–5393.

15 P. C. Li, J. Wu, Z. Wu, Y. M. Jia, J. P. Ma, W. P. Chen, L. H. Zhang, J. Yang and Y. S. Liu, Strong tribocatalytic dye decomposition through utilizing triboelectric energy of barium strontium titanate nanoparticles, *Nano Energy*, 2019, **63**, 103832.

16 S. Wu, C. Z. Sun, X. F. Yang, C. Z. Hu, L. J. Liu and L. Fang, Effect of strontium substitution on the structure and dielectric properties of unfilled tungsten bronze $Ba_{4-x}Sr_xSmFe_{0.5}Nb_{9.5}O_{30}$ ceramics, *Ceram. Int.*, 2020, **46**, 9240–9248.

17 G. Zerihun, G. S. Gong, S. Huang and S. L. Yuan, Dielectric relaxation and ferroelectric phase transition in $Sr_4BiRTi_4Nb_6O_{30}$ (R = Sm, Eu) ceramics, *Curr. Appl. Phys.*, 2016, **16**, 843–849.

18 C. Z. Hu, Z. Sun, Q. H. Zhu, C. C. Li, L. J. Liu and L. Fang, Temperature-stable unfilled tungsten bronze dielectric ceramics: $Ba_{3.5}Sm_{1.5}Fe_{0.75}Nb_{9.25}O_{30}$, *Int. J. Appl. Ceram. Technol.*, 2017, **14**, 269–273.

19 X. Zhu, M. Fu, M. C. Stennett, P. M. Vilarinho, I. Levin, C. A. Randall, J. Gardner, F. D. Morrison and I. M. Reaney, A crystal-chemical framework for relaxor versus normal ferroelectric behavior in tetragonal tungsten bronzes, *Chem. Mater.*, 2015, **27**, 3250–3261.

20 C. Z. Hu, L. J. Hou, L. Fang and L. J. Liu, Preparation and dielectric properties of unfilled tungsten bronze ferroelectrics $Ba_4RETiNb_9O_{30}$, *J. Alloys Compd.*, 2013, **581**, 547–552.

21 J. Gardner and F. D. Morrison, A-site size effect in a family of unfilled ferroelectric tetragonal tungsten bronzes: $Ba_4R_{0.67}Nb_{10}O_{30}$ (R = La, Nd, Sm, Gd, Dy and Y), *Dalton Trans.*, 2014, **43**, 11687–11695.

22 W. B. Feng, X. L. Zhu, X. Q. Liu and X. M. Chen, Crystal structure, ferroelectricity and polar order in $Ba_4R_2Zr_4Nb_6O_{30}$ (R = La, Nd, Sm) tetragonal tungsten bronze new system, *J. Mater. Chem. C*, 2017, **5**, 4009–4016.

23 A. Kudo and Y. Miseki, Heterogeneous photocatalyst materials for water splitting, *Chem. Soc. Rev.*, 2009, **38**, 253–278.

24 M. k. Tian, W. F. Shang guan, J. Yuan, L. Jiang, M. X. Chen, J. W. Shi, Z. Y. Ou yang and S. J. Wang, $K_4Ce_2M_{10}O_{30}$ (M = Ta, Nb) as visible-light-driven photocatalysts for hydrogen evolution from water decomposition, *Appl. Catal., A*, 2006, **309**, 76–84.

25 X. Huang, K. Wang, Y. Wang, B. Wang, L. Zhang, F. Gao, Y. Zhao, W. Feng, S. Zhang and P. Liu, Enhanced charge carrier separation to improve hydrogen production efficiency by ferroelectric spontaneous polarization electric field, *Appl. Catal., B*, 2018, **227**, 322–329.

26 W. Zhang, X. Y. Pan, P. Q. Long, X. T. Liu, X. Long, Y. Yu and Z. G. Yi, Platinum nanoparticles supported on defective tungsten bronze-type $KSr_2Nb_5O_{15}$ as novel photocatalyst for efficient ethylene oxidation, *J. Mater. Chem. A*, 2017, **5**, 18998–19006.

27 T. Takayama, K. Tanabe, K. Saito, A. Iwase and A. Kudo, The $KCaSrTa_5O_{15}$ photocatalyst with tungsten bronze structure for water splitting and CO_2 reduction, *Phys. Chem. Chem. Phys.*, 2014, **16**, 24417–24422.

28 C. Z. Sun, X. Y. Guo, R. Ji, C. Z. Hu, L. J. Liu, L. Fang, Z. X. Cheng and N. N. Luo, Strong tribocatalytic dye degradation by tungsten bronze $Ba_4Nd_2Fe_2Nb_8O_{30}$, *Ceram. Int.*, 2021, **47**, 5038–5043.

29 Z. Wang, W. H. Ma, C. C. Chen, H. Ji and J. Zhao, Probing paramagnetic species in titania based heterogeneous photocatalysis by electron spin resonance (ESR) spectroscopy – a mini review, *Chem. Eng. J.*, 2011, **170**, 353–362.

30 Y. Y. Wu, Y. Z. Zhou, H. Xu, Q. Q. Liu, Y. Li, L. L. Zhang, H. Q. Liu, Z. G. Tu, X. N. Cheng and J. Yang, Highly active, superstable, and biocompatible Ag/polydopamine/g-C_3N_4 bactericidal photocatalyst: synthesis, characterization, and mechanism, *ACS Sustainable Chem. Eng.*, 2018, **6**, 14082–14094.

31 B. R. Xu, Y. D. Li, Y. Q. Gao, S. Liu, D. Lv, S. J. Zhao, H. Gao, G. Q. Yang, N. Li and L. Ge, Ag–AgI/Bi_3O_4Cl for efficient visible light photocatalytic degradation of methyl orange: the surface plasmon resonance effect of Ag and mechanism insight, *Appl. Catal., B*, 2019, **246**, 140–148.

32 T. Xu, Y. Cai and K. E. O'Shea, Adsorption and photocatalyzed oxidation of methylated arsenic species in TiO_2 suspensions, *Environ. Sci. Technol.*, 2007, **41**, 5471–5477.

33 E. Gao and W. Wang, Role of graphene on the surface chemical reactions of $BiPO_4$–rGO with low OH-related defects, *Nanoscale*, 2013, **5**, 11248–11256.

34 Y. M. Liu, X. Y. Wang, Y. M. Qiao, M. D. Min, L. Wang, H. Shan, Y. L. Ma, W. Hao, P. Tao, W. Shang, J. B. Wu, C. G. Song and T. Deng, Pyroelectric synthesis of metal–$BaTiO_3$ hybrid nanoparticles with enhanced pyrocatalytic performance, *ACS Sustainable Chem. Eng.*, 2019, **7**, 2602–2609.

35 O. Lobacheva, Y. M. Yiu, N. Chen, T. K. Sham and L. V. Goncharova, Changes in local surface structure and Sr depletion in Fe-implanted $SrTiO_3$ (001), *Appl. Surf. Sci.*, 2017, **393**, 74–81.

36 H. Brunckova, M. Kanuchova, H. Kolev, E. Mudra and L. Medvecky, XPS characterization of $SmNbO_4$ and $SmTaO_4$ precursors prepared by sol–gel method, *Appl. Surf. Sci.*, 2019, **473**, 1–5.

37 S. Tu, H. Huang, T. Zhang and Y. Zhang, Controllable synthesis of multi-responsive ferroelectric layered perovskite-like $Bi_4Ti_3O_{12}$: photocatalysis and piezoelectric catalysis and mechanism insight, *Appl. Catal., B*, 2017, **219**, 550–562.

38 Y. Yao, Y. Cai, F. Lu, F. Wei, X. Wang and S. Wang, Magnetic recoverable $MnFe_2O_4$ and $MnFe_2O_4$–graphene hybrid asheterogeneous catalysts of peroxymonosulfate activation for efficient degradation of aqueous organic pollutants, *J. Hazard. Mater.*, 2014, **270**, 61–70.

39 X. Li and Y. Ye, Photocatalytic degradation of rhodamine B over $Pb_3Nb_4O_{13}$/fumed SiO_2 composite under visible light irradiation, *J. Phys. Chem. C*, 2007, **111**, 13109–13116.

40 C. L. Yu, G. Li, L. F. Wei, Q. Z. Fan, Q. Shu and J. C. Yu, Fabrication, characterization of β-MnO_2 microrod catalysts

and their performance in rapid degradation of dyes of high concentration, *Catal. Today*, 2014, **224**, 154–162.

41 A. Zhang, Z. Liu, B. Xie, J. Lu, K. Guo, S. Ke, L. Shu and H. Fan, Vibration catalysis of eco-friendly $Na_{0.5}K_{0.5}NbO_3$-based piezoelectric: an efficient phase boundary catalyst, *Appl. Catal., B*, 2020, **279**, 119353.

42 C. Hu, H. Huang, F. Chen, Y. Zhang, H. Yu and T. Ma, Coupling piezocatalysis and photocatalysis in Bi_4NbO_8X (X = Cl, Br) polar single crystals, *Adv. Funct. Mater.*, 2020, **30**, 1908168.

43 H. T. Baytekin, B. Baytekin, J. T. Incorvati and B. A. Grzybowski, Material transfer and polarity reversal in contact charging, *Angew. Chem., Int. Ed.*, 2012, **51**, 4843–4847.

44 B. Baytekin, H. T. Baytekin and B. A. Grzybowski, What really drives chemical reactions on contact charged surfaces?, *J. Am. Chem. Soc.*, 2012, **134**, 7223–7226.

45 D. J. Lacks and R. M. Sankaran, Contact electrification of insulating materials, *J. Phys. D: Appl. Phys.*, 2011, **44**, 453001.

46 S. H. Pan and Z. Zhang, Fundamental theories and basic principles of triboelectric effect: a review, *Friction*, 2019, **7**, 2–17.

47 S. Horikoshi, H. Hidaka and N. Serpone, Hydroxyl radicals in microwave photocatalysis. Enhanced formation of OH radicals probed by ESR techniques in microwave-assisted photocatalysis in aqueous TiO_2 dispersions, *Chem. Phys. Lett.*, 2003, **376**, 475–480.

48 D. N. Liu, D. Y. Chen, N. J. Li, Q. F. Xu, H. Li, J. H. He and J. M. Lu, Surface engineering of g-C_3N_4 by stacked BiOBr sheets rich in oxygen vacancies for boosting photocatalytic performance, *Angew. Chem.*, 2020, **132**, 4549–4554.

49 C. Liu, H. J. Zhu, Y. S. Zhu, P. Y. Dong, H. J. Hou, Q. X. Xu, X. W. Chen, X. G. Xi and W. H. Hou, Ordered layered N-doped $KTiNbO_5$/g-C_3N_4 heterojunction with enhanced visible light photocatalytic activity, *Appl. Catal., B*, 2018, **228**, 54–63.

50 M. Wang, G. Q. Tan, D. Zhang, B. Li, L. Lv, Y. Wang, H. J. Ren, X. L. Zheng, A. Xia and Y. Liu, Defect-mediated Z-scheme $BiO_{2-x}/Bi_2O_{2.75}$ photocatalyst for full spectrum solar-driven organic dyes degradation, *Appl. Catal., B*, 2019, **254**, 98–112.

51 T. Takata, S. Ikeda, A. Tanaka, M. Hara, J. N. Kondo and K. Domen, Mechano-catalytic overall water splitting on some oxides(II), *Appl. Catal., A*, 2000, **200**, 255–262.

52 X. L. Xu, Z. Wu, L. B. Xiao, Y. M. Jia, J. P. Ma, F. F. Wang, L. Wang, M. S. Wang and H. T. Huang, Strong piezo-electro-chemical effect of piezoelectric $BaTiO_3$ nanofibers for vibration-catalysis, *J. Alloys Compd.*, 2018, **762**, 915–921.

53 L. Parizot, T. Chave, M. Galvez, H. Dutilleul, P. Costa and S. Nikitenko, Sonocatalytic, oxidation of EDTA in aqueous solutions over noble metal-free Co_3O_4/TiO_2 catalyst, *Appl. Catal., B*, 2019, **241**, 570–577.

54 S. Zhang, Z. Liu, M. Ruan, Z. Guo, E. Lei, W. Zhao, D. Zhao, X. Wu and D. Chen, Enhanced piezoelectric-effect-assisted photoelectrochemical performance in ZnO modified with dual cocatalysts, *Appl. Catal., B*, 2020, **262**, 118279.